# Surface-wave analysis for static corrections in mineral exploration: A case study from central Sweden

Myrto Papadopoulou[1]*, Federico Da Col[1], Binbin Mi[2], Emma Bäckström[3], Paul Marsden[3], Bojan Brodic[4], Alireza Malehmir[4] and Laura Valentina Socco[1]

[1]*Politecnico di Torino, Department of Environment, Land and Infrastructure Engineering, Torino, Italy*, [2]*Zhejiang University, Hangzhou, Zhejiang, China*, [3]*Nordic Iron Ore, Ludvika, Sweden, and* [4]*Uppsala University, Uppsala, Sweden*

## ABSTRACT

In mineral exploration, increased interest towards deeper mineralizations makes seismic methods attractive. One of the critical steps in seismic processing workflows is the static correction, which is applied to correct the effect of the shallow, highly heterogeneous subsurface layers, and improve the imaging of deeper targets. We showed an effective approach to estimate the statics, based on the analysis of surface waves (groundroll) contained in the seismic reflection data, and we applied it to a legacy seismic line acquired at the iron-oxide mining site of Ludvika in Sweden. We applied surface-wave methods that were originally developed for hydrocarbon exploration, modified as a step-by-step workflow to suit the different geologic context of hard-rock sites. The workflow starts with the detection of sharp lateral variations in the subsurface, the existence of which is common at hard-rock sites. Their location is subsequently used, to ensure that the dispersion curves extracted from the data are not affected by strong lateral variations of the subsurface properties. The dispersion curves are picked automatically, windowing the data and applying a wavefield transform. A pseudo-2D time-average S-wave velocity and time-average P-wave velocity profile are obtained directly from the dispersion curves, after inverting only a reference curve. The time-average P-wave velocity profile is then used for the direct estimation of the one-way traveltime, which provides the static corrections. The resulting P-wave statics from the field data were compared with statics computed through conventional P-wave tomography. Their difference was mostly negligible with more than 91% of the estimations being in agreement with the conventional statics, proving the effectiveness of the proposed workflow. The application of the statics obtained from surface waves provided a stacked section comparable with that obtained by applying tomostatics.

**Key words:** Surface waves, Statics, Mining.

## INTRODUCTION

Hard-rock sites, the typical geological setting of the majority of mineral deposits, have been the targets of exploration with geophysical methods in the last decades (Eaton, Milkereit and Salisbury 2003 and references therein). The recent increase in interest towards deeper mineralizations makes seismic methods attractive. As a consequence, the development of effective seismic processing techniques is important (Malehmir *et al.* 2012). In land seismic reflection, a critical step of the processing workflow is the static corrections (statics). They are applied on the seismic data to correct for the effect of

*E-mail: myrto.papadopoulou@studenti.polito.it

near-surface heterogeneities and varying low-velocity over-burden thicknesses, which can distort the body-wave (BW) field, affecting the final seismic image (e.g. Rogers 1981; Cox 1999). Static corrections are therefore a key processing step, which increases the quality and resolution of the seismic sections, improving the interpretation of the final result (Marsden 1993). Several methods can be used to estimate the near-surface velocity model, needed for computing static corrections, the most common of which is first-break tomography. A possible estimation approach is to use the surface waves (SW), contained in the reflection seismic data (Foti *et al.* 2014).

Surface-wave methods are based on the analysis of the dispersive characteristics of the propagating wavefield, which are extracted from the seismic data as curves relating the phase velocity and frequency of SWs, known as dispersion curves (DC). SW may propagate at different modes that appear as different branches of the DC (Aki and Richards 1980). SW DCs are obtained by processing active- or passive-source seismic data, typically applying a wavefield transform. They are then inverted for S-wave velocity ($V_S$); several studies, though, suggest their use also for P-wave velocity ($V_P$) estimation (e.g. Maraschini, Boiero and Socco 2009; Socco and Comina 2017). Oil and gas seismic exploration is mainly based on the analysis of BW. As a result, the acquisition is usually optimized to obtain BWs, and SWs are treated as noise and filtered out in the data-processing stage. However, their sensitivity to the velocity of the shallow subsurface makes them a potentially valuable by-product that can be used for the estimation of statics, directly from exploration data, without the need of extra, costly data acquisitions (e.g. Soumya, Stewart and Al Dulaijan 2010; Boiero *et al.* 2011; Douma and Haney 2011; Miao *et al.* 2016).

On the other hand, the application of SW analysis to mineral exploration remains limited and, to the authors' knowledge, there are no recent publications referring to the use of active-source SW data at hard-rock sites for statics estimation. In fact, from an extensive literature search concerning SW-related publications in the last five years in the most popular repositories for applied geophysics (EAGE EarthDoc and SEG Digital Library), only 6% of published papers on SWs refer to applications to stiff sites (Fig. 1). Most of these focus on the use of SWs for seismic site characterization and seismic-response evaluation. In total, fewer than 2% of the SW-related publications refer to mining and mineral-exploration applications. This lack of related published research can be attributed to several challenges that arise when analysing SWs at mining sites.
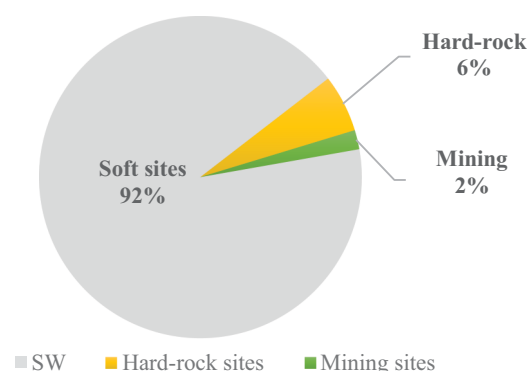


**Figure 1** Publications (journal papers and expanded abstracts) on EAGE's 'Earthdoc' and 'SEG digital library' from January 2014 to December 2018. From a total number of 480 SW-related publications, 92% refer to soft sites, 6% to hard-rock sites and 2% to mining and mineral-exploration sites.

The quality of SW analysis can be severely affected by the noise, originated by mining activities (e.g. mining operations, crushers, blasting and drilling), which might present high amplitude and broad frequency band (Urosevic *et al.* 2007; Górszczyk, Malinowski and Bellefleur 2015).

The nature of the near surface can be significantly variable, including outcrops of the crystalline bedrock, layers of weathering materials of variable thickness (Eaton *et al.* 2003) and extreme surface conditions, such as swampy soils (Malehmir *et al.* 2017) or dense vegetation and forests (Saunders, Lamb and Sweeney 1991). Moreover, hard-rock environments are characterized by heterogeneities, such as fractures and faults (Buske, Bellefleur and Malehmir 2015), as well as rough topography (e.g. Heinonen *et al.* 2011). Other heterogeneities, such as mined blocks, on-going and/or abandoned mining workings, roads, tunnels and other local subsurface targets are also common in mining sites (e.g. Hollis *et al.* 2018). These highly heterogeneous near-surface conditions impose limitations to typical SW methods which assume a locally 1D subsurface.

Acquisition may be limited by the rough terrain and minesite restrictions, causing the sources and receivers to be irregularly positioned (Nedimović and West 2003; Harrison, Urosevic and Stoltz 2007). This affects multichannel SW processing, which is based on 2D wavefield transforms of seismic data obtained from multiple receivers located in-line with the sources.

Another restriction is the choice of the source, which might be limited to explosive shots in drilled shot holes, due to irregular surface conditions (e.g. Roberts *et al.* 1997; L'Heureux, Milkereit and Adam 2005). However, burying the

source can cause a strong reduction of the energy transformed into SWs (Foti *et al.* 2018), making their analysis challenging.

In crystalline environments, sharp velocity contrasts are present, if a soft, weathering layer covers the stiff bedrock. This can cause the excitation of higher modes of SWs or other types of guided waves (Bergamo, Comina and Maraschini 2011), which can be dominant over a large frequency band, leading to a misidentification of the fundamental mode.

Despite these difficulties, valuable information can be gained from SW data at hard-rock sites. The experience of utilizing SWs in different fields of applications where hard rocks are present (e.g. seismic site characterization and geotechnical engineering) serves as proof of concept. For example, Pileggi *et al.* (2011) showed that SW analysis at hard-rock sites benefits from the high velocity of the subsurface, due to which, longer wavelengths are generated, causing the investigation depth to be higher (80–100 m in their examples). The same authors showed, by means of numerical simulations, that the SW content of the ambient vibration field increases with increasing bedrock depth. Useful guidelines were proposed by Cercato *et al.* (2010), who dealt with shallow-bedrock examples, and proposed muting the data to separate the SW fundamental mode from other waves that are generated due to the property contrast. Casto *et al.* (2009) underlined the need to use all available *a priori* information, to better constrain the bedrock depth in SW inversion.

In the field of mineral exploration, some promising examples show the benefits of using SWs. Recently, Hollis *et al.* (2018) showed that the long wavelengths estimated with ambient-noise SW tomography can indicate the geological boundary of a mineral deposit. Sharma, Hollis and McBride (2018) confirmed that ambient-noise SW recordings provide great investigation depths and estimated a 1D $V_S$ profile at a mineral exploration site. Several case studies at mining sites dealt with the existence of sharp lateral heterogeneities and showed that they can be delineated, using certain properties of SWs. For example, Rector *et al.* (2015) applied active SW tomography introducing a new acquisition scheme to image old mine workings. They showed that SW phase velocities and amplitudes are sensitive to the presence of these kinds of voids. Similar conclusions about the sensitivity of SWs were made by Sherman *et al.* (2014) and Ivanov, Miller and Peterie (2016) who applied SW-based methods for locating voids and mine workings in historical mining sites.

In the current work, we used a legacy data set from the Blötberget iron-oxide mining area of Ludvika mines in central Sweden. Production of the mine was abandoned

during the late 1970s, but there has been renewed interest, due to technological advancements and favourable market conditions, initiating many research activities. Two high-resolution active-source seismic field campaigns (in 2015 and 2016) were carried out. The acquisition details of the 2015 survey and results are given in Malehmir *et al.* (2017). The 2016 data set is currently the subject of various studies, including conventional processing by Markovic *et al.* (2020), prestack depth imaging by Bräunig *et al.* (2020) and surface-wave interferometry and adaptive subtraction by Balestrini *et al.* (2020).

The aim of the current study is to provide a workflow for statics estimation, which can be used to improve the mineralization imaging, using groundroll-related noise. The processing workflow consists of SW-based methods, originally developed for soft-site characterization, and accounts for the characteristics of the data to suit the different geologic context of hard-rock sites. Data processing starts with a method for the detection of sharp lateral variations. The DCs are then picked along the survey line with an automated method, stacking shot gathers to improve S/N. Following the methods outlined in Socco, Comina and Khosro Anjom (2017) and Socco and Comina (2017), we obtain a pseudo-2D time-average $V_S$ ($V_{Sz}$) and time-average $V_P$ ($V_{Pz}$) profile. The latter is used for the direct estimation of the one-way time, which provides the static corrections. The workflow is fast, compared with tomostatics, which requires first-break picking, and to typical SW methods, which usually require excessive iterative inversion processes. Here inversion is run only on a reference DC, and the rest of the applied processes are based on computationally efficient data transformations.

## SITE DESCRIPTION

The area of Blötberget in central Sweden (Fig. 2) belongs to the historical mineral district of Bergslagen, which is known for its high-quality iron-oxide deposits (Malehmir *et al.* 2017). The mineralization consists mainly of magnetite and hematite, with presence of apatite and quartz and calc-silicate minerals. It exists as two separate sheet-like mineralized horizons, hosted by volcanic rocks. They moderately dip (about 45°) towards the southwest, to a known depth of at least 800 to 850 m.

Maries *et al.* (2017) provided a detailed description of the downhole and laboratory measurements of the physical properties of the mineralization and host rocks from seven drilled boreholes. Laboratory measurements (density, rock-quality designation and magnetite content) were made on the core

**(a)**



**(b)**
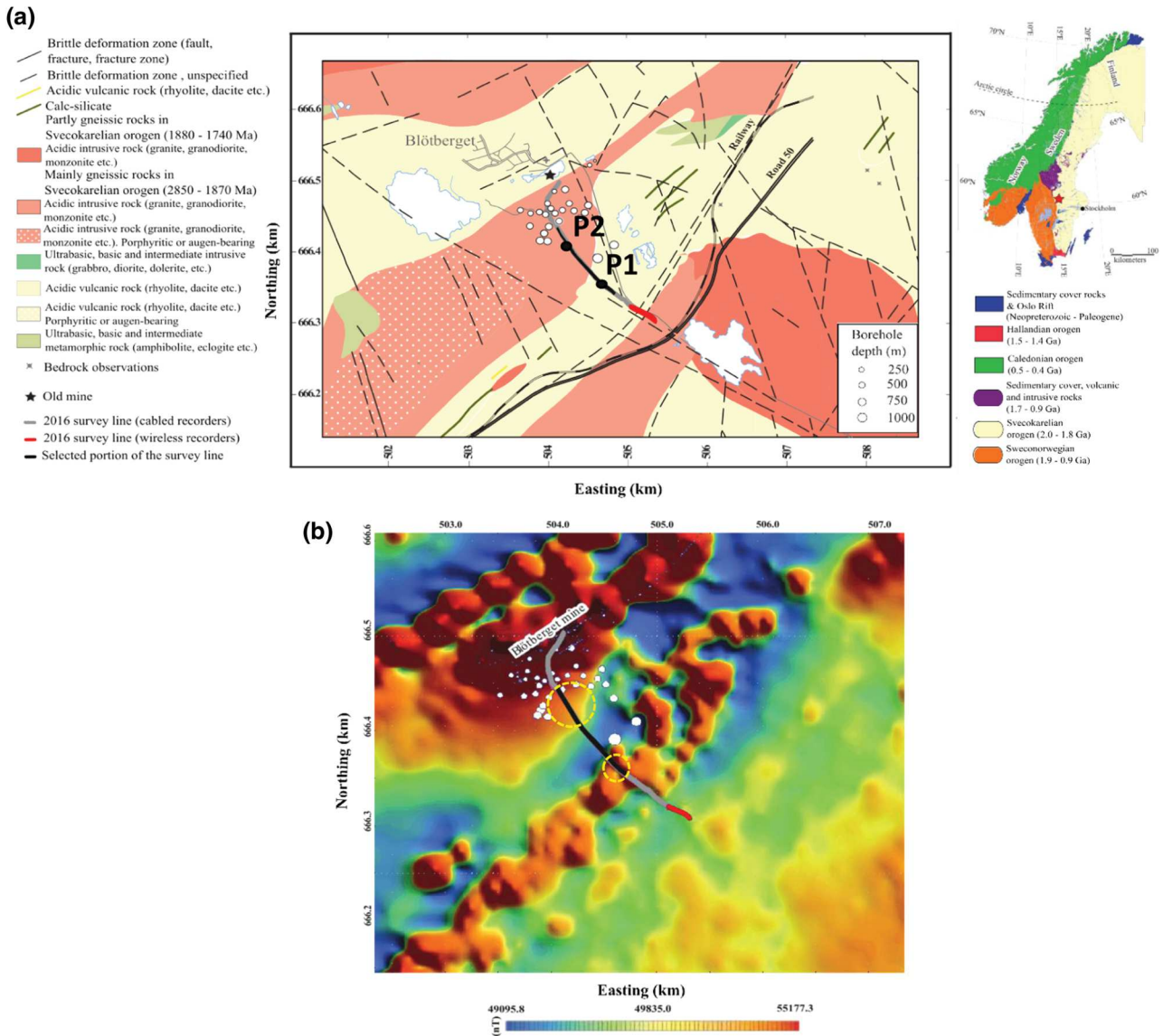


**Figure 2** (a) Geological map of the Blötberget area in central Sweden showing the location of the seismic profile of the 2016 survey (grey for the cabled and red for the wireless recorders) and existing boreholes intersecting the mineralization. The portion of the data set analysed in the current work is plotted in black. Points 'P1' and 'P2' represent the shot positions of the seismic records shown in Fig. 5. (b) Total-field aeromagnetic map of the Blötberget area in central Sweden showing the location of the seismic profile and existing boreholes. The survey line of 2016 is plotted in grey (cabled recorders) and red (wireless recorders). The portion of the profile studied in this work (black) intersects two magnetic lineaments, in the positions given by the yellow circles. The geological and total-field magnetic maps were kindly provided by the Geological Survey of Sweden.

samples from the mineralization, while, downhole logging (full-waveform triple sonic, natural gamma, magnetic susceptibility, formation resistivity, fluid temperature and conductivity) was performed throughout the full borehole lengths, including the near surface. The logging measurements showed that the first 100 m consists mainly of stiff materials, such as metasedimentary argillitic layers and granite, with $V_S$ ranging

between 3000 and 4000 m/s, $V_P$ between 4500 and 6500 m/s and density between 2500 and 3000 kg/m$^3$.

## EXPERIMENTAL DATA

The seismic profile of 2016 is given in grey and red in Fig 2(a,b). The data were recorded using 10-Hz cabled
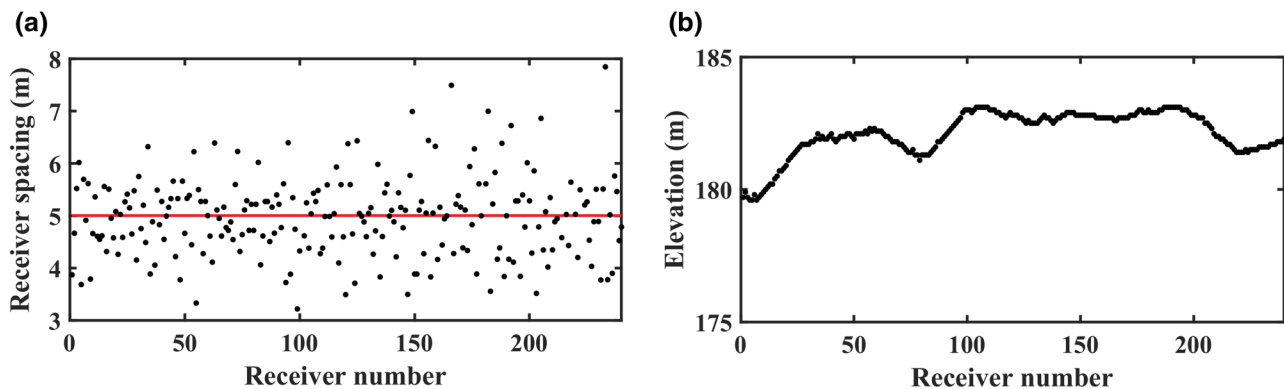
**(a)**



**(b)**



**Figure 3** (a) Spacing between the used receivers (black dots), compared with the nominal value of 5 m (red line). (b) Elevation of the used receivers.

geophones spaced at 5 m (grey), and 10-Hz wireless stations spaced at 10 m (red) with a 500-kg Bobcat-mounted drophammer as the source. The recorded time made available was 10 s (reduced to 2 s for processing) and the sampling rate was 1 ms. Preliminary analysis showed that the recordings of the 5 m-spaced receivers gave the best-quality SWs, and they were chosen for the analysis. From these, we used only a portion, where shots and receivers are in-line and the changes in the elevation are minimal, compared with the receiver spacing. The part of the data set that was analysed, counts for 240 shots and 240 receivers (total length of 1200 m) and is plotted in black in Fig. 2(a,b). The distance between all consecutive receivers is plotted in Fig. 3(a), where one can observe fluctuations from the nominal value of 5 m (red line), caused by acquisition restrictions. These were accounted for in the processing workflow. In Fig. 3(b), we show the elevation of each receiver. The maximum elevation difference among all the receivers is 3.6 m and, therefore, we considered flat topography during processing. In Fig. 4 we show examples of normalized amplitude spectra computed for different offsets, which reveal that the data contain dominant frequencies up to 90 Hz, with a peak at approximately 35 Hz.

The data quality for SW analysis is highly heterogeneous along the line. In Fig. 5(a,c), we present two examples of raw shot gathers: Fig. 5(a) shows a high-quality gather (in terms of SW analysis) and Fig. 5(c) a low-quality one. Their frequency-phase velocity spectra are given in Fig. 5(b,d), where the extracted DCs, corresponding to the spectra maxima, are plotted in black. In Fig. 5(a), the SWs (indicated by the yellow lines) are dominant and they show a weak dispersion. The spectrum (Fig. 5b) presents clear maxima of a single propagation mode, that is weakly dispersive at high phase velocities, ranging from 1900 to 2700 m/s. In Fig. 5(c), the SWs (indicated by the yellow dashed lines) are not easy to be recognized in

the gather and the resulting DC (Fig. 5d) is narrow-banded and noisy. All these aspects were taken into account for the data-processing workflow.

## PROCESSING WORKFLOW AND RESULTS

A schematic representation of the processing workflow that was applied to the data set to estimate the statics is given in Fig. 6.

### Identification of sharp lateral variations

Surface wave (SW) methods, which assume 1D models, can also be applied when the subsurface properties present smooth lateral variations, if the DCs are extracted using a windowing technique (Bohlen *et al.* 2004; Boiero and Socco 2010). However, if there are sharp discontinuities, their location should be identified before processing, to avoid having erroneous DCs. Two methods were applied to identify the location of possible variations: the decay exponent ($\gamma$) and the attenuation coefficient ($a$) method. Both methods were introduced by Nasseri-Moghaddam, Cascante and Hutchinson (2005) and extended to multifold data analysis by Bergamo and Socco (2014), who implemented the codes used in our work. According to Colombero *et al.* (2017), the methods are complementary, and their joint interpretation increases the robustness of the results.

The decay exponent method is based on the fact that, for a laterally homogeneous medium with no intrinsic attenuation, the energy decay exponent of SWs is equal to one, following the equation of geometrical spreading (Richart, Hall and Woods 1970). Compensating for the geometrical spreading, $\gamma$ becomes zero. Strong deviations from this theoretical value are associated with back-reflections or attenuations of energy,
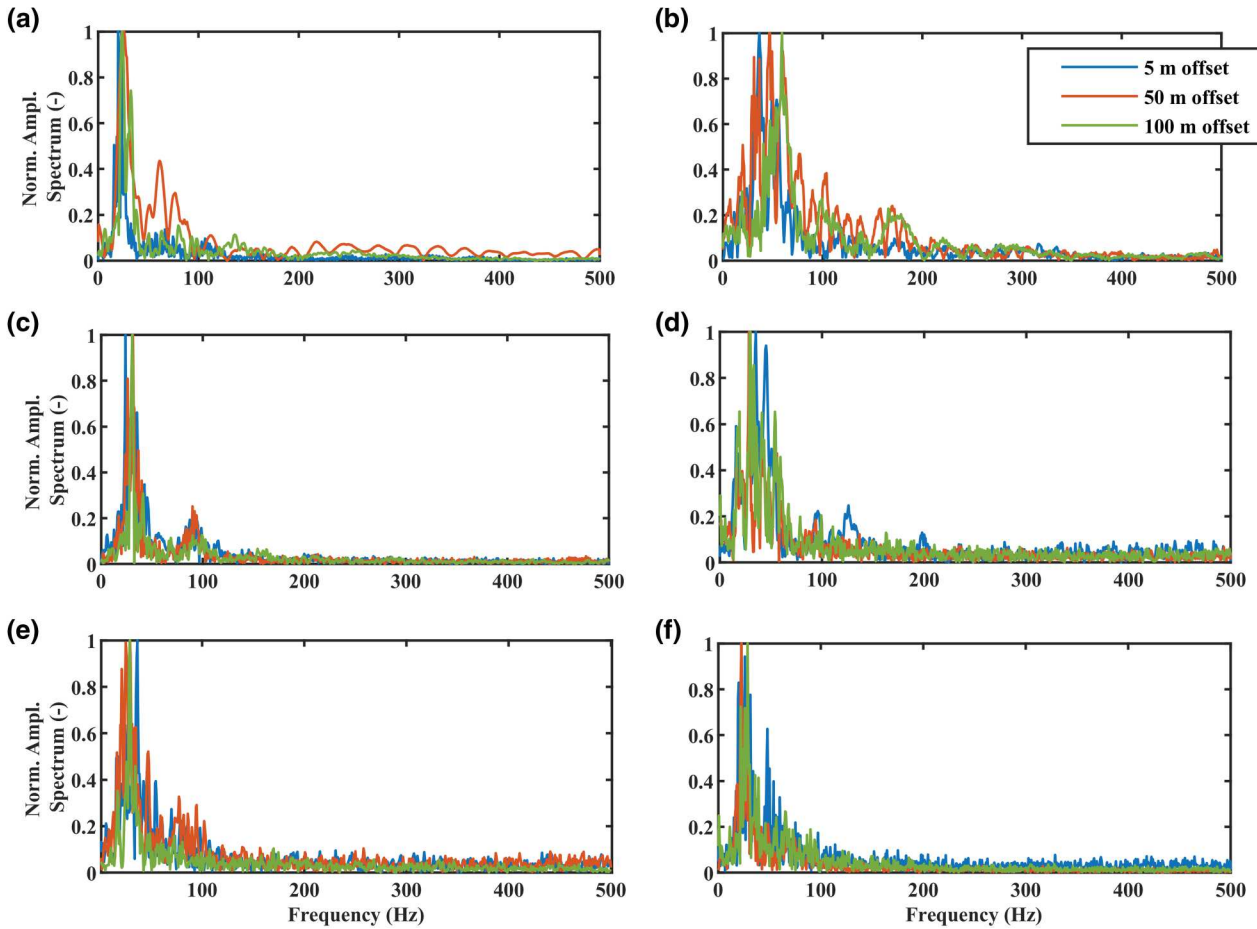
**Figure 4** Normalized amplitude spectra of the shots at position (a) 85 m, (b) 285 m, (c) 500 m, (d) 750 m, (e) 900 m and (f) 1000 m.

caused by subsurface discontinuities. The decay exponent, $\gamma$, can be computed according to

$$\frac{E_i}{E_{i+1}} = \left(\frac{r_i}{r_{i+1}}\right)^{-\gamma}, \tag{1}$$

where $r_i$ and $r_{i+1}$ are the distances from the shots and $E_i$ and $E_{i+1}$ are the energy values for the receivers $i$ and $i+1$, respectively. For multifold implementation, $\gamma$ is computed in a moving window along the seismic line. The size of the window is a compromise between the noise that can locally affect the trace energy and the lateral resolution. After testing different sizes, we selected a window of 11 receivers (55 m), which was the narrowest window with acceptable noise. The window was moved by a step of 10 m. The average and standard deviation of $\gamma$ from shots inside all windows were computed, distinguishing between positive ($\gamma_{pos}$) and negative ($\gamma_{neg}$) offset traces, which, according to Bergamo and Socco (2014), show opposite behaviour when strong heterogeneities are encountered by the SWs, and should be examined together, to

improve the interpretation of the results. The standard deviation provides a measure of uncertainty. In Fig. 7(a), we show the plot of $\gamma_{pos}$ (red) and $\gamma_{neg}$ (blue) versus the receiver positions, and the standard deviations are given by the error bars.

The attenuation coefficient method estimates the location of subsurface discontinuities based on significant variations of $\alpha$, because these variations are caused by back reflections or attenuations of the energy of the waves, due to sharp subsurface discontinuities. The attenuation coefficient, $\alpha$, is computed for couples of receivers, located at distances $r_i$ and $r_{i+1}$ from each shot at each frequency $f_j$, after compensating for the geometrical spreading, according to

$$E_{j,i+1} = E_{j,i}e^{-2\alpha_j(r_{i+1}-r_i)}. \tag{2}$$

Since the energy in this method is computed frequency by frequency, the results indicate the frequency (wavelength) band that is affected by the energy variations and, therefore,
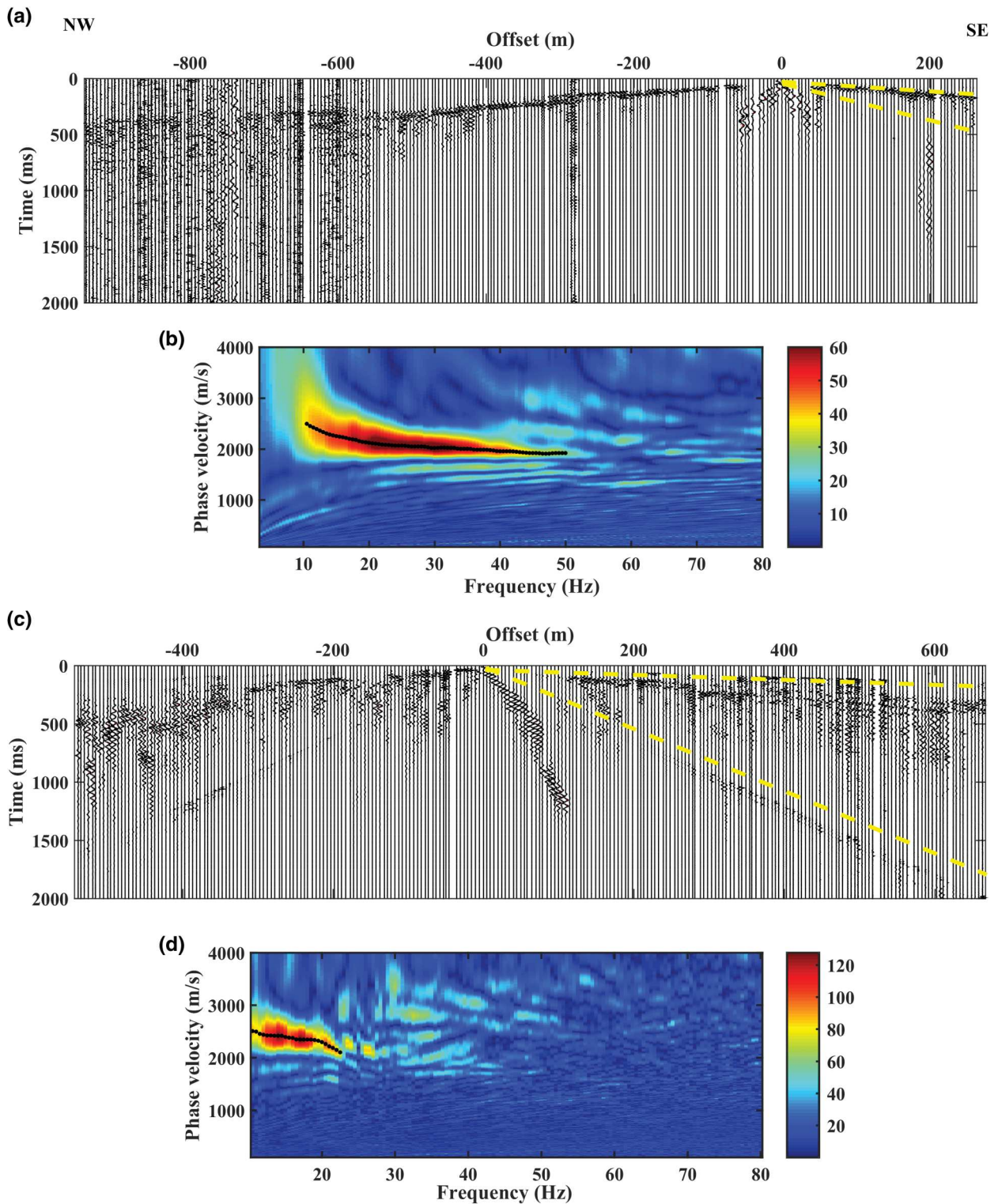
**Figure 5** (a) Example raw shot gather, corresponding to the position of point 'P1' in Fig. 2(a) and (b) its frequency–phase velocity spectrum, considering the positive-offset receivers. (c) Another example raw shot gather (point 'P2' in Fig. 2a) and (d) its frequency–phase velocity spectrum, considering the positive-offset receivers. In (a,c), the yellow dashed lines indicate the surface waves. In (b,d), the black lines indicate the picked DCs.
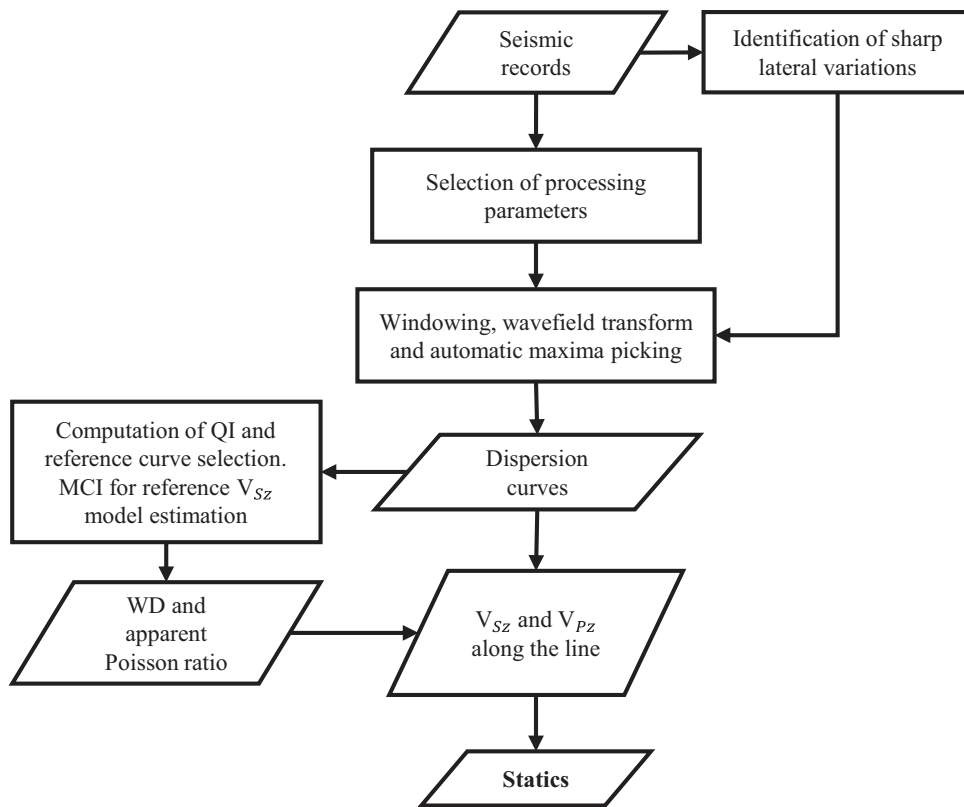
**Figure 6** Scheme of the SW processing workflow applied on the portion of the data set to obtain $V_P$ static corrections.

provide a qualitative indication of the depth of the subsurface discontinuities. For the multifold implementation, we computed $\alpha$ inside a moving window of 11 receivers, for which $\alpha$ was averaged and normalized to the related standard deviations, distinguishing for positive- and negative-offset traces. The average normalized $\alpha$ for positive-offset traces ($\alpha_{pos}$) and negative-offset traces ($\alpha_{neg}$) were stacked, to remove the effect of the source position, as proposed by Colombero *et al.* (2017). The resulting stacked normalized $\alpha$ is given by the colour scale in the plot of Fig. 7(b).

We examine the results of the two methods together, to identify the critical zones, where strong anomalies are present. As shown in Fig. 7(a), the black lines, labelled from '2' to '8', mark positions where $\gamma_{pos}$ and $\gamma_{neg}$ present the most prominent peaks and show opposite sign. At the same positions, again marked by the black lines in Fig. 7(b), $\alpha$ presents sharp increases. These strong energy contrasts can be associated with sudden changes in the subsurface properties (e.g. fractured zones, changes in lithology and man-made structures). Their positions (Table 1) were stored, to be excluded from the extraction of the DC.

The green and orange boxes in Fig. 7(a,b) define two areas where both methods show continuous energy anomalies. In Fig. 7(a), the green box defines an area, 316 m long, where $\gamma_{pos}$ fluctuates constantly and $\gamma_{neg}$ never reaches negative values, indicating strong energy attenuation. In the same location, $\alpha$ (Fig. 7b) also shows constant energy fluctuations that end at the right boundary of the green box, labelled as '1'. In the SE end of the line, $\gamma$ and $\alpha$ present anomalies with long lateral extent (126 m). No local peaks can be found in $\gamma$, and the anomalies of $\alpha$ are continuous. The boundary of this transition is the left-hand side of the orange box, labelled as '9' in Fig. 7(a,b). The positions of boundaries '1' and '9' (Table 1) were stored, to be omitted from the DC extraction.

**Extraction of the dispersion curves**

In order to obtain a set of DCs that provide information of possible smooth variations of the subsurface properties, we used the algorithm implemented by Socco *et al.* (2009). It applies a spatial window on the seismic traces, and spans all trace positions, to extract local DCs. The extraction is made
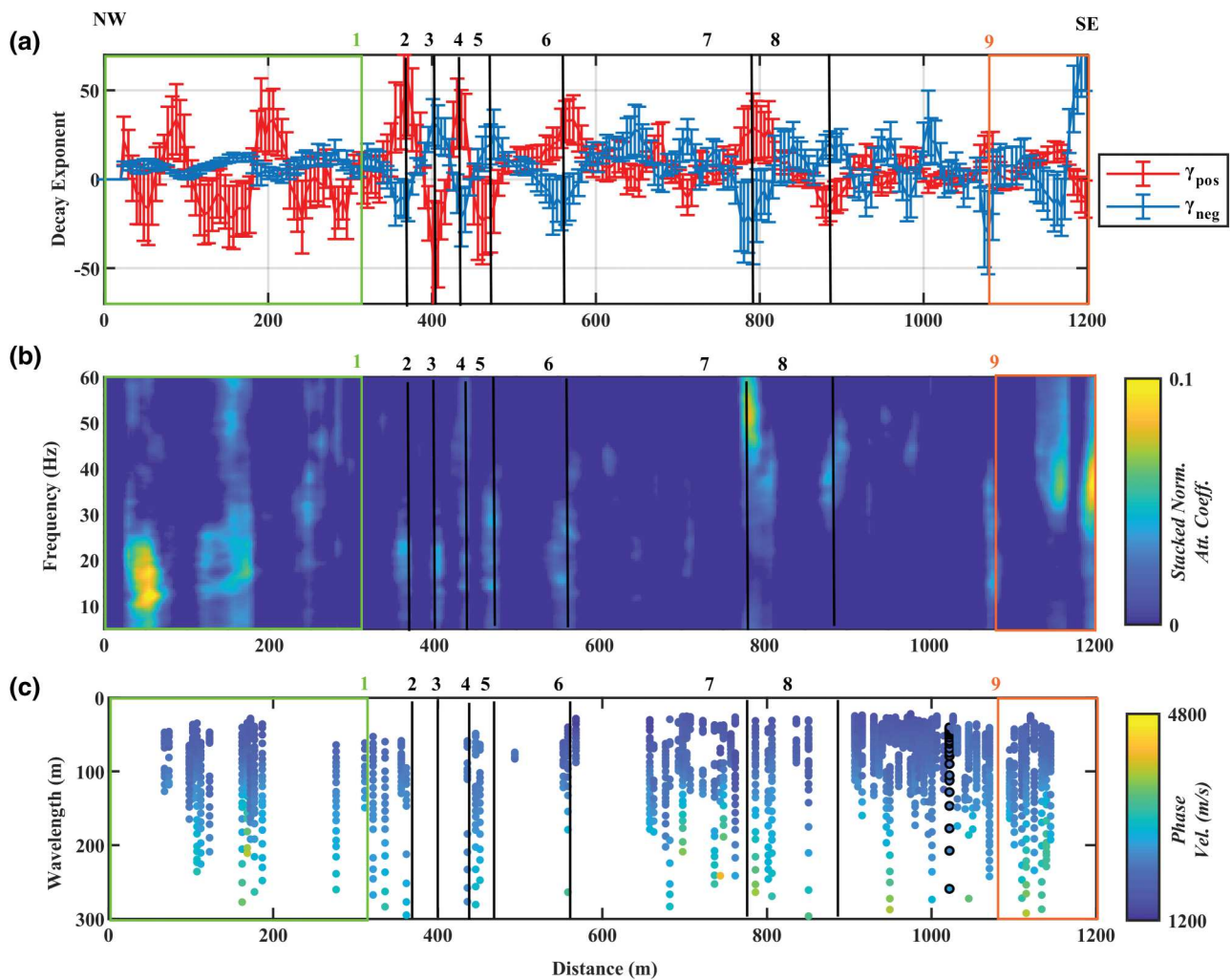
**Figure 7** (a) Average decay exponent estimated along the seismic line for positive-offset traces (blue line) and negative-offset traces (red line). (b) Stacked normalized attenuation coefficient. (c) Eighty dispersion curves extracted along the seismic line. The vertical axis represents the wavelength while the colour scale provides the phase velocity, given by the colour bar. With black edges shown in (c), we present the dispersion curve at position 1022 m, which was chosen as reference for the estimation of the W/D relationship. The black lines and green and orange boxes in all panels indicate the locations of sharp energy anomalies.

by picking the maxima of the spectrum, after stacking several shot spectra, to improve S/N. The optimum processing parameters for the DC extraction (window length, minimum and maximum offset between the window and the sources and step of the moving window) were decided according to tests on sample shot records. The samples were randomly chosen from three different areas along the line, located between positions 0–365 m, 568–791 m and 882–1073 m. This was done to test the window length using receivers, that do not cross any of the sharp lateral variations, marked by the black lines and the edges of the green and orange boxes in Fig. 7(a,b). For the spectrum computation, we transformed the data in

the frequency–phase velocity (*f-v*) domain, according to Park, Miller and Xia (1998), because this wavefield transform can be applied to irregularly spaced receivers (Fig. 3a).

The optimal window length was chosen as a compromise between the improved spectral resolution, given by a long window, and the noise introduced, when far-offset traces were included. The choice of the minimum and maximum offset between the sources and the window provided the offset range in which shots could be used for stacking. The offset range selection was aimed at avoiding near-field effects and ensuring that the far-offset traces still contained high S/N SWs. The number of spectra to be stacked within the chosen offset range was

**Table 1** Estimated location of sharp lateral variations

| Sharp lateral variation | Position on the seismic line (m) |
| --- | --- |
| 1 | 316 |
| 2 | 366 |
| 3 | 407 |
| 4 | 436 |
| 5 | 461 |
| 6 | 567 |
| 7 | 792 |
| 8 | 881 |
| 9 | 1074 |

a trade-off between improved S/N and computational cost. The step of the moving windows worked as a compromise between the number of DCs along the line and the sensitivity of the DCs to lateral heterogeneity. The final chosen windowing parameters are presented in Table 2.

To optimize the automatic procedure of the DC extraction, a 'mask' was defined, to select the spectral region, where the energy maxima corresponding to the DC lie. At each location, a DC was extracted by automatically picking the spectral maxima inside the 'mask'. The position of each DC was assigned to the centre of the window. DCs at the positions, indicated by the black lines and by the edges of the green and orange boxes in Fig. 7(a,b), were disregarded. In total, a set of 80 DCs were extracted along the line and are plotted in wavelength–phase velocity domain, along the 2D line in Fig. 7(c), and in frequency–phase velocity domain in Fig. 8(a).

In Fig. 7(c), each DC is plotted at the location corresponding to the centre of the window, and the vertical axis represents the wavelength. The phase velocity is given by the colour scale. The spatial distribution of the DCs varies significantly along the line, and there exists several gaps. Some of these gaps correspond to the positions of the sharp lateral variations as estimated by $\gamma$ (Fig. 7a) and $\alpha$ (Fig. 7b). The additional gaps correspond to positions where the spectra did not present clear maxima and, therefore, no DC could be picked.

**Table 2** Windowing parameters for the DC extraction

| Processing parameter | Value |
| --- | --- |
| Window size | 75 m |
| Step | 15 m |
| Minimum offset | 10 m |
| Maximum offset | 300 m |
| Number of stacked shots | 1–58 |

## Reference curve selection and Monte Carlo inversion and reference $V_{Sz}$ model estimation

For the selection of the reference DC, we followed the strategy of Socco *et al.* (2017), who showed that the impact of the reference DC selection on the final result is low (2%–10%), even at sites with lateral $V_S$ variability (150%), as long as the curves overlap or present a smooth phase–velocity transitions. Only if there are strong variations in the shape, and/or velocity range of the curves, which can be detected visually by plotting all the DCs together, is it necessary to split them in different groups and process them separately. In our case, we selected only one reference DC, since they are all concentrated in one frequency and phase–velocity region, as shown in Fig. 8(a), with no obvious separation in different groups. The lateral variability of $V_S$ can be approximated by the lateral variability of the phase velocity, which is at maximum 80%, as shown in Fig. 8(b). As a further check, we ran a clustering algorithm over the DC set (not shown) that confirmed that the DCs group in a single cluster.

The selection of the reference DC was based on the quality of the DCs given by the frequency band, standard deviation, and difference between the DCs of single positive- and negative-offset shots. We computed the quality index (QI), based on Karimpour (2018), as follows:

$$QI = 1 - \frac{(NSD + ND_{PN} + NFB)}{\max(NSD + ND_{PN} + NFB)}, \qquad (3)$$

where NSD is the standard deviation of each DC, with respect to the DCs of the individual shots used for spectral stacking, summed for all frequency components and normalized to the maximum standard deviation; $ND_{PN}$ is the difference of the average DCs extracted from positive- and negative-offset shots, summed for each frequency and normalized to the maximum difference and NFB is the reciprocal of the frequency band (FB) of each DC, normalized to the maximum of all the FBs. The plot of QI is given in Fig. 9. The DC with the highest QI value is the one at position 1022 m (noted by the black circle in Fig. 9 and highlighted with the black edges in Fig. 7c and plotted as a black curve in Fig. 8a), and it was the one chosen as reference.

We inverted the reference DC using the Monte Carlo algorithm of Socco and Boiero (2008). For the Monte Carlo inversion, one million profiles were randomly generated simulating a three-layered model (two layers plus half space). The layer thickness and $V_S$ were randomly sampled, within the model space boundaries, plotted in Fig. 10a (blue dashed lines). The density was fixed at 2000 kg/m³ for the shallow layers and 2800 kg/m³ for the half space. The Poisson's ratio
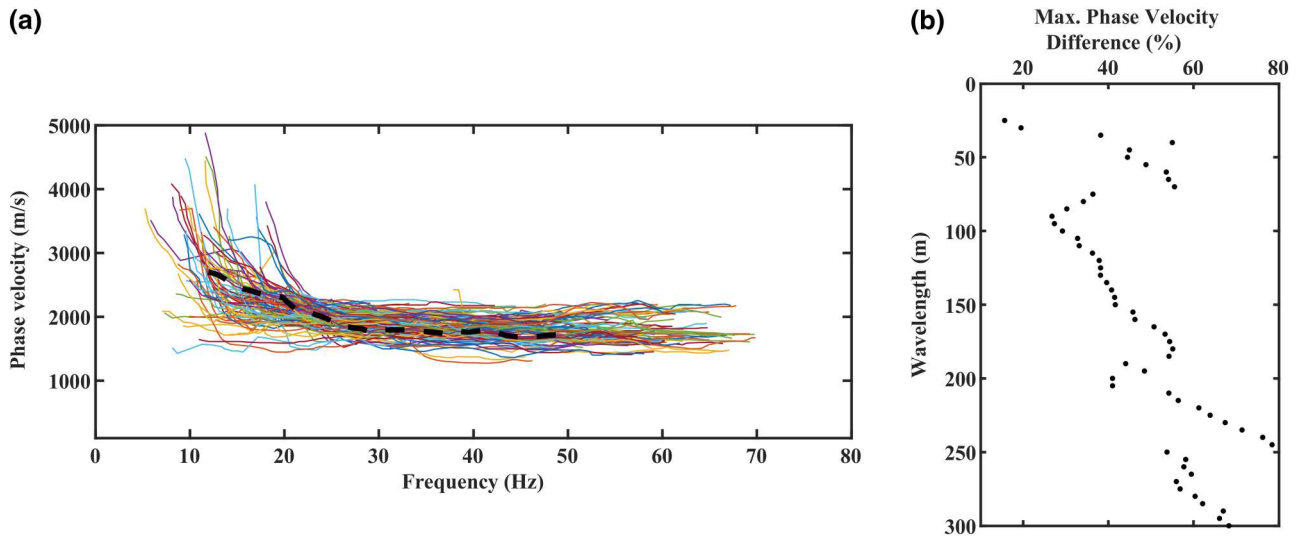
**(a)**



**(b)**



**Figure 8** (a) Eighty DCs picked along the portion of the seismic line. Different colours correspond to different positions and the DC that was chosen as reference (located at offset position 1022 m) is given in dashed black. (b) Maximum phase velocity variability at each wavelength of all the extracted DCs.

for all the layers was randomly sampled from a wide range (0.1–0.45), which is reasonable for near-surface materials (e.g. Gercek 2007).

In Fig. 10(a), we present the accepted models, with a colour scale that indicates the misfit between their synthetic DCs and the experimental DC. The DCs of the best-fitting models are presented in Fig. 10(b) (using the same colour scale), compared with the experimental one (black dots). The best-fitting model is given in red (Fig. 10a), and it was transformed into time-average $V_S$ ($V_{Sz}$) according to

$$V_{Sz} = \frac{\sum_n h_i}{\sum_n \frac{h_i}{V_{Si}}}, \qquad (4)$$

where $h_i$ is the thickness and $V_{Si}$ the S-wave velocity of the $i$th layer, and $n$ is the number of layers down to each depth ($z$) of the profile.

**Wavelength–depth relationship and apparent Poisson's ratio estimation**

The time-average $V_S$ ($V_{Sz}$) model (black line in Fig. 11a) was compared with the reference DC (black dots in Fig. 11a) to obtain the wavelength and depth couples for which $V_{Sz}$ and phase velocity are equal, as described in Socco *et al.* (2017), for the entire thickness of the inverted $V_S$ model (red line in Fig. 11a). The couples were interpolated with a polynomial fit, to obtain the wavelength–depth (W/D) relationship, which is plotted in Fig. 11(b) (black line).

According to Socco and Comina (2017), the W/D relationship is sensitive to the Poisson's ratio, allowing its estimation. This was achieved by means of a sensitivity analysis: for the same $V_S$ profile, we simulated different W/D relationships (different colours in Fig. 12a), each time changing the value of the Poisson's ratio from 0.1 to 0.45 with a step of 0.05. The experimental W/D curve (black dashed line in Fig. 12a) was
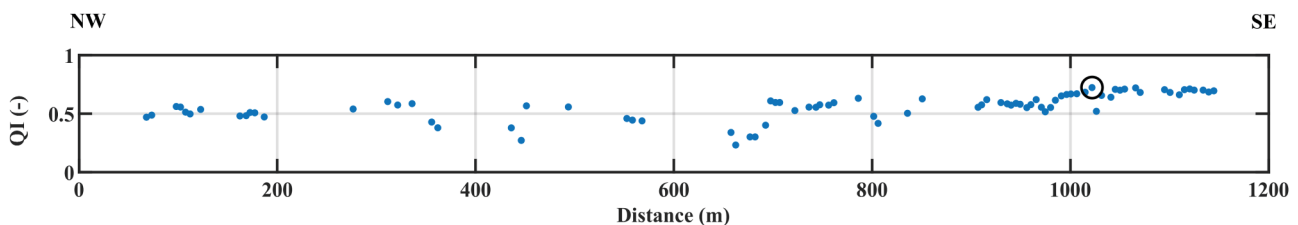


**Figure 9** Quality index (QI) of the extracted DCs (blue dots). The highest QI value, corresponding to the reference DC, is circled in black.
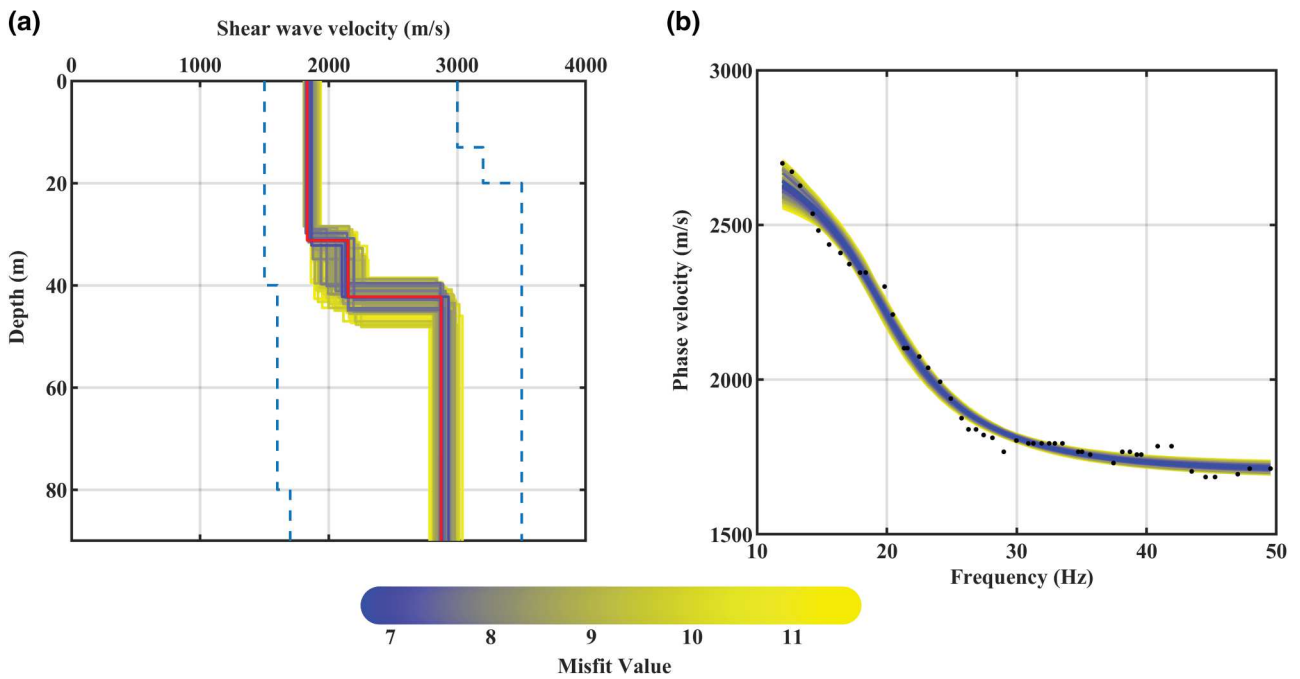
**Figure 10** Monte Carlo inversion results. (a) Best-fitting profiles selected by the inversion. Red colour represents the best-fitting profile. The blue dashed lines give the model parameter space. (b) Synthetic DC of the best-fitting models compared with the experimental DC (black points). The colour scale in both panels indicates the misfit and is given by the colour bar.

compared with the simulated ones, providing the apparent Poisson's ratio profile ($v_z$), that is, the Poisson's ratio that relates the time-average $V_S$ ($V_{Sz}$) with the time-average $V_P$ ($V_{Pz}$) profile, which is given in Fig. 12(b).

**Wavelength–depth transformation, time-average P-wave velocity and statics estimation**

The W/D relationship of the reference model was used to transform all the other DCs into $V_{Sz}$. For each DC, we
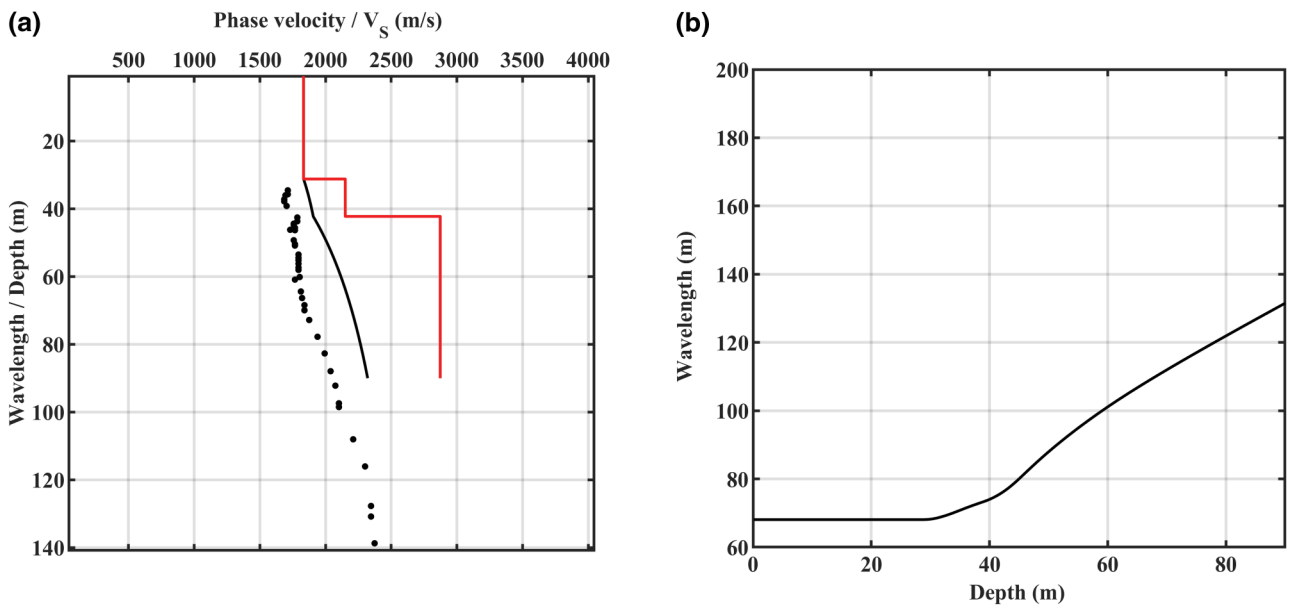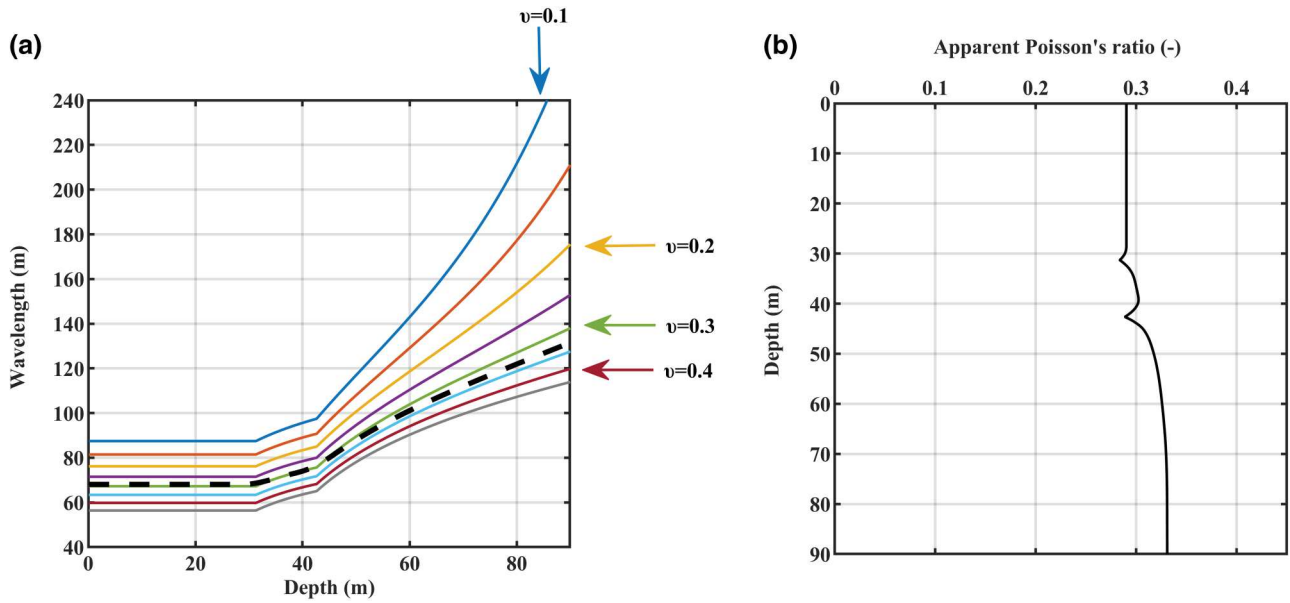


**Figure 11** (a) Reference 1D $V_S$ model (red line), reference $V_{Sz}$ model (black line) and reference DC (black dots). (b) Experimental W/D curve.

**Figure 12** (a) The curve of the experimental W/D (black dashed) is compared with synthetic W/D curves (different colours, depending on the Poisson's ratio). (b) Apparent Poisson's ratio profile, that is, the Poisson's ratio that relates the time-average $V_S$ ($V_{Sz}$) with the time-average $V_S$ ($V_{Pz}$).

converted the wavelength components into their corresponding depth values from the W/D and, for each couple, the $V_{Sz}$ was set equal to the phase velocity. The resulting 1D $V_{Sz}$ profiles are plotted in Fig. 13(a) along the seismic line, at the positions of their corresponding DCs. The vertical axis represents the depth, and the $V_{Sz}$ is given by the colour scale. The depth of each profile depends on the wavelength of its corresponding DC.

According to Socco and Comina (2017), the expected lateral variability of the Poisson's ratio is low if the variability of $V_S$ is low. Thus, the estimated apparent Poisson's ratio profile was used to obtain $V_{Pz}$ from all the estimated $V_{Sz}$ profiles along the seismic line. The $V_{Pz}$ model was estimated from the $V_{Sz}$ 1D profiles at each position $j$ ($V_{Szj}$) and the apparent Poisson's ratio ($v_z$), according to the following relationship (Socco and Comina 2017):

$$V_{Pzj} = V_{Szj}\sqrt{\frac{2v_z - 2}{2v_z - 1}}. \qquad (5)$$

The estimated $V_{Pz}$ profile is given in Fig. 13(b).

Finally, the computation of the one-way time (static shift) at each position $j$ was carried out using the values of each 1D $V_{Pz}$ profile at a (floating) datum plan $z_d$ according to

$$t_{z_dj} = \frac{z_d}{V_{P_{z_dj}}}, \qquad (6)$$

where $t_{Z_{dj}}$ is the one-way time and $V_{P_{Z_{dj}}}$ is the time-average P-wave velocity at position $j$ and depth $z_d$. To obtain the source and receiver statics, the one-way times estimated along the line were interpolated. The statics can be obtained for any datum down to the investigation depth, which here is 90 m. In Fig. 14(a,b), in red we show the resulting one-way time for two example datum depths, 40 and 50 m, respectively, which are both deeper than the known bedrock depth.

## DISCUSSION

We presented a workflow of SW methods to estimate $V_P$ static corrections, using an example from the iron-oxide mining site of Ludvika in Sweden.

The two methods for the detection of sharp lateral variations identified several locations where local heterogeneities are present (labelled from '1' to '9' in Fig. 7) and the DCs from these locations were excluded from the analysis.

The energy anomalies, marked by black lines in Fig. 7(a,b), are sharp and well separated from each other, presenting narrow lateral extent. We compare them to the results of Colombero *et al.* (2017), who proved, using a synthetic model, that at the interfaces between materials with different properties, $\gamma_{pos}$ and $\gamma_{neg}$ present a strong separation, their sign depending on the type of contrast, and $\alpha$ takes high
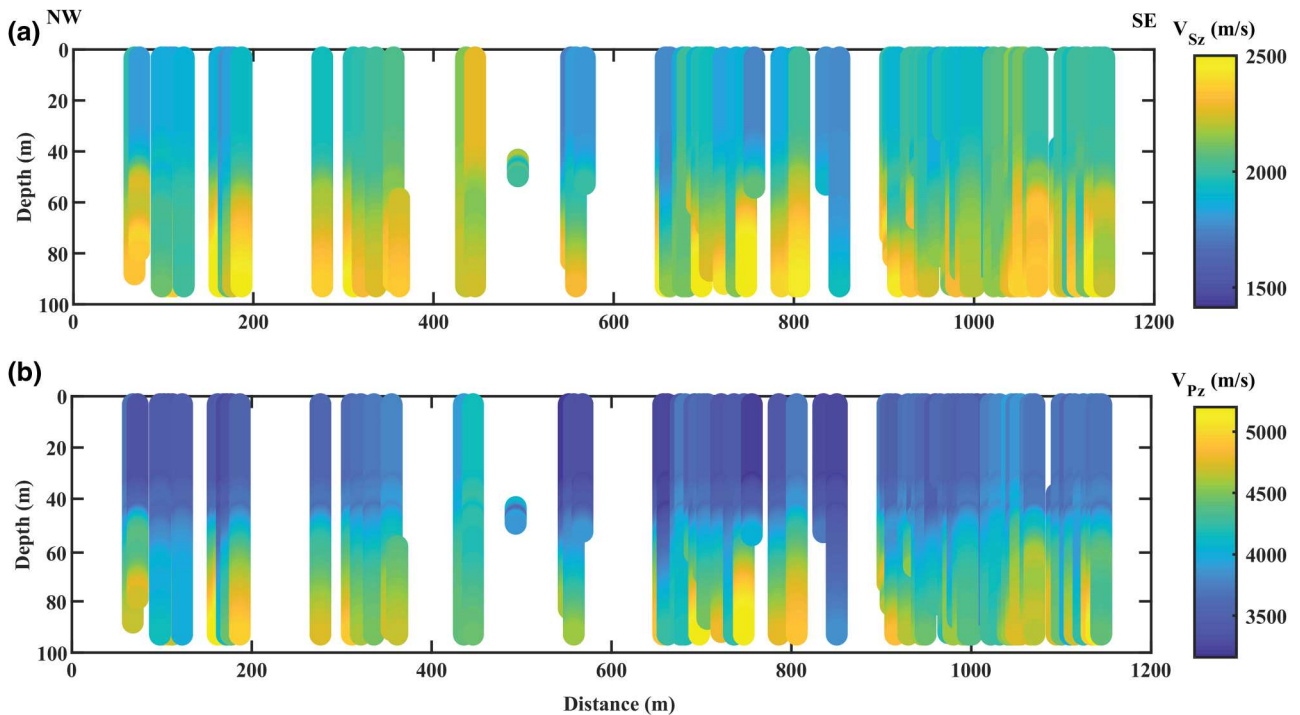
**Figure 13** (a) Time-average $V_S$ ($V_{Sz}$) model and (b) time-average $V_P$ ($V_{Pz}$) model obtained by the applied workflow. The thickness of the 1D models is illustrative.

values at the position of the interface. Lines '2'–'5' are at a small distance from each other (41 m between '2' and '3', 29 m '3' and '4' and 25 m between '4' and '5'), which is lower than the length of the window used for $\gamma$ and $\alpha$ computation (55 m) and higher than the window step (10 m). Therefore, we cannot distinguish between the contributions of each discontinuity. Because, as can be seen in Fig. 7(b), they affect low frequencies (mostly < 40 Hz) and because a water stream crosses the line at this location, we can conclude that these anomalies are all probably related to the shallow fracturing of the rock. The area between lines '6' and '7' is probably the shallow expression of a fault, which was identified by Bräunig *et al.* (2020), and causes attenuation of the propagating SW energy. The energy anomaly of line '8' presents a narrower separation between $\gamma_{pos}$ and $\gamma_{neg}$, with respect to all the other black lines, and $\alpha$ shows a peak only at high frequencies (> 30 Hz), meaning that the heterogeneity is very shallow. A possible cause can be the local reduction of the bedrock depth, creating a velocity contrast at shallow depths.

The anomalies marked by the green and orange boxes in Fig 7(a,b) have longer lateral extent and, thus, they are probably related to large-scale geological features. A comparison with the total-field aeromagnetic data map (Fig. 2b) reveals that at the NW and SE ends, the selected portion of the

seismic line intersects two magnetic lineaments, which correspond to oxide-bearing formations, in the positions shown by the yellow circles in Fig. 2(b). Hence, we can assume that the energy anomalies bounded by the boxes are related to the shallow expression (highly fractured zones) of deeper mineralized bodies.

The applied processing workflow allowed the extraction of a great number of DCs, 75% of which present a quality index value higher than 0.5 (Fig. 9). However, the poor data quality could not be mitigated at all positions, resulting in the gaps that can be observed in Fig. 7(c). The DCs present some lateral variability of the phase velocity at each wavelength, which is, however, always below 80% (Fig. 8b). Moreover, there is no obvious separation of the DCs in the frequency–phase velocity domain (Fig. 8a). This proves that the DCs do not belong to strongly heterogeneous geological environments and justifies the choice of one reference DC, used only for the application of W/D data transform.

The estimated $V_{Sz}$ along the line (Fig. 13a) ranges between 1400 and 2500 m/s, indicating the existence of materials with high $V_S$ in the near surface, in agreement with the geological information of the site (Maries *et al.* 2017).

Regarding our estimation of $\upsilon_z$ (Fig. 12b), although it cannot be directly compared with the local measurements of
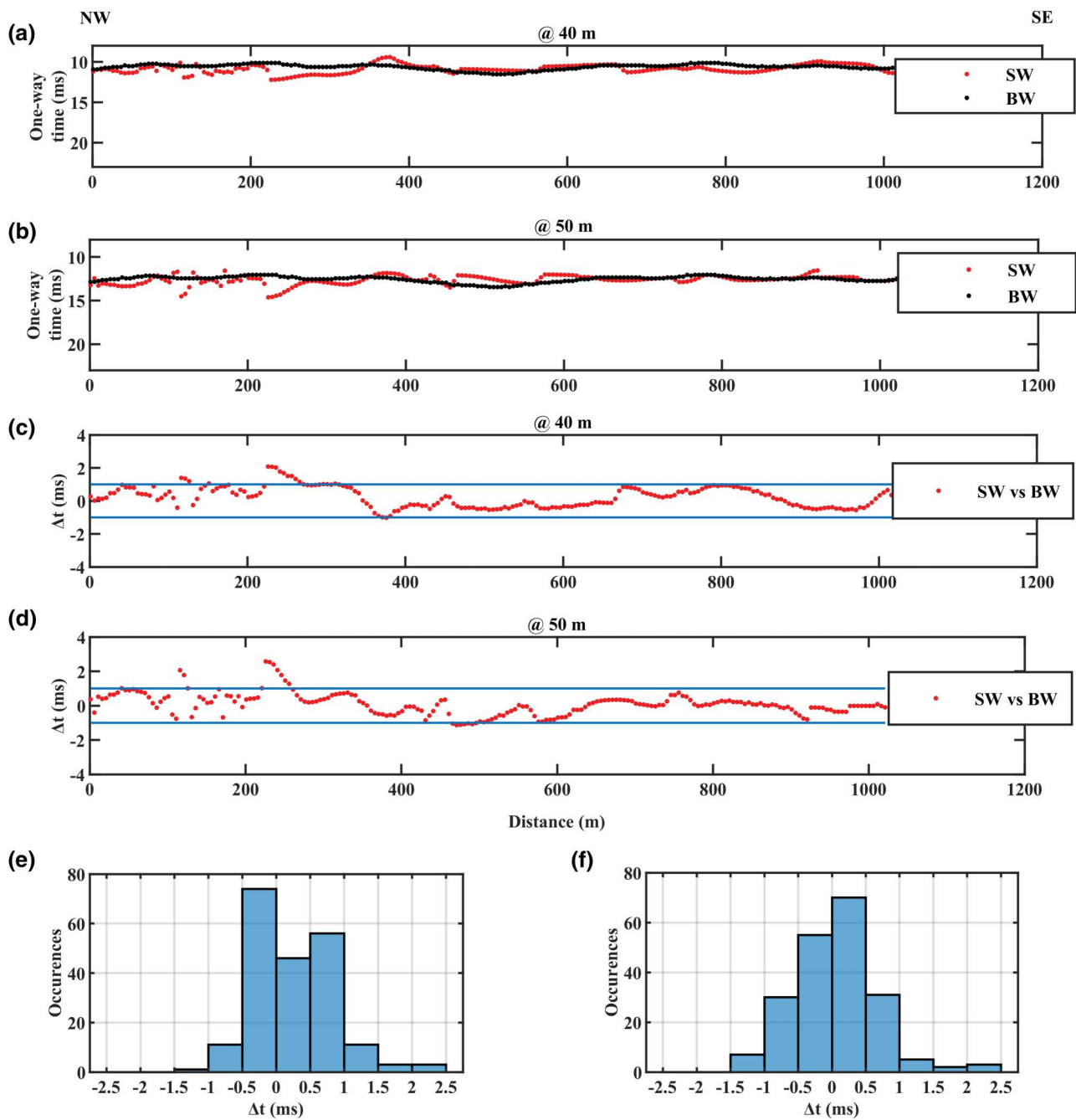
**Figure 14** One-way time (static shift) at a datum depth of (a) 40 m and (b) 50 m. In red, the statics from SW direct $V_{P_z}$ estimation of our workflow and in black, the tomostatics (Bräunig *et al.* 2020). One-way time difference between SW direct $V_{P_z}$ estimation and tomostatics at a datum depth of (c) 40 m and (d) 50 m. Distribution of the one-way time difference ($\Delta t$) between the SW direct $V_{P_z}$ estimation of our workflow and tomostatics at a datum depth of (e) 40 m and (f) 50 m. The sum of occurrences in (e) and (f) is 205.

the Poisson's ratio from the site, because $\upsilon_z$ is by its nature a smooth profile, our estimation lies within reasonable values, according to Maries *et al.* (2017), who show values of the Poisson's ratio in the range between 0.05 and 0.35.

In Fig. 14, we compare our estimated statics with the tomostatics obtained by Bräunig *et al.* (2020), who applied first-break traveltime tomography on the same data set. Being an accepted method for near-surface $V_P$ estimation, BW
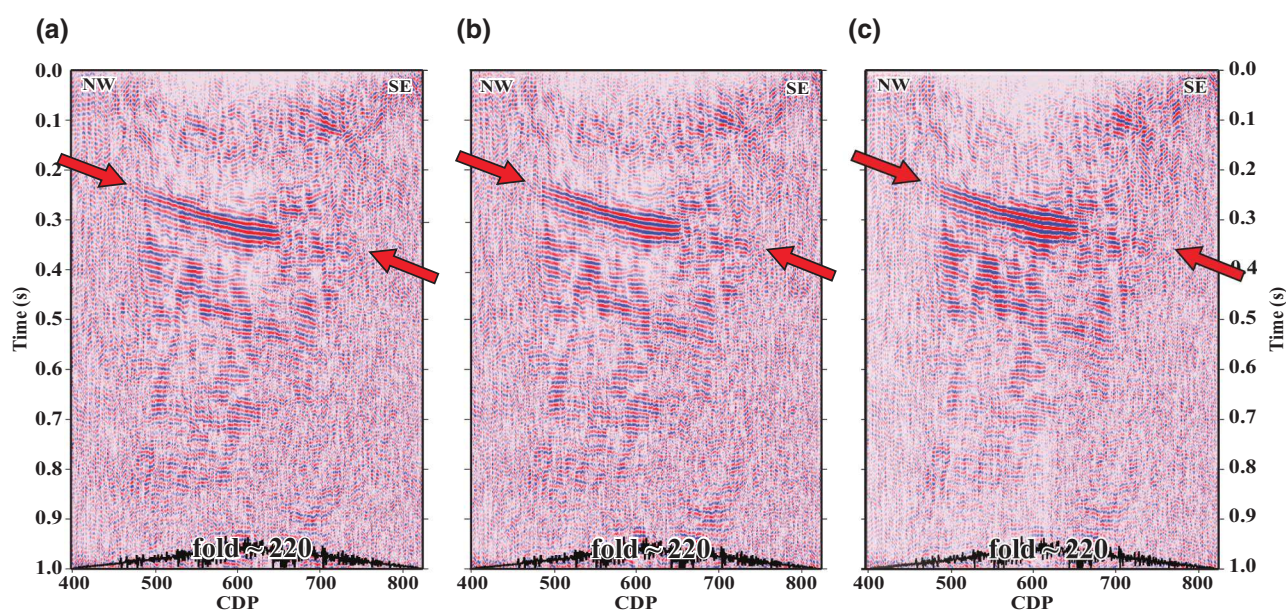
**Figure 15** Brute stack (a) before any statics, (b) after application of static corrections obtained by P-wave traveltime tomography and (c) after application of static corrections obtained by our method.

tomography serves as our benchmark. We compare the statics at two datum plans (40 m, shown in Fig. 14a and 50 m, shown in Fig. 14b), which were chosen as examples, because they are deeper than the known depth of the bedrock. We show in red the statics resulting from our workflow and in black the ones from BW tomography. In Fig. 14(c,d), we show the difference of the one-way time estimations for the two datum depths. The blue lines define the interval of $\pm 1$ ms (equal to the sampling rate), within which we consider the difference negligible. According to the histogram of Fig. 14(e), 7.8% of the measurements present a difference that is out of the range of $\pm 1$ ms for the computation at 40 m datum, while for the 50 m datum, 8.29% are out of $\pm 1$ ms range (Fig. 14f). The comparison confirms that our direct estimation presents a low error with respect to the benchmark.

In Fig. 15(a), we show the stacked section before any statics. The resulting brute stacks, after the application of the tomostatics and of our workflow's statics at 40 m datum, are shown in Fig. 15(b,c), respectively. It can be observed that our statics resulted in an improved coherency of the reflector (indicated by the red arrows) with respect to the section with no statics, while, a slight improvement can also be detected with respect to the tomostatics. We can therefore conclude that the proposed SW-based workflow is a valid alternative to the conventional method of statics estimation, which is completely independent from BW data and, therefore, can be useful when obtaining BW is less effective (e.g.

when first-break traveltimes cannot be easily picked due to noise).

The workflow is fast compared with the conventional method (tomostatics), which requires first-break picking. Moreover, it is faster than the typical SW methods, since most of the processes (estimation of the W/D relationship and the apparent Poisson's ratio, transformation of all the DCs into $V_{Sz}$ and $V_{Pz}$ and computation of statics) are automatized procedures, based only on data transforms, which require very little computational effort. Indeed, all the computations were performed in a few minutes. The methods for the detection of sharp lateral variations and the process for the extraction of the DCs are completely automatic, except for some preliminary tests required for processing parameter selection. The only computationally demanding task is the inversion of the reference DC, which required 2 hours to run on a standard workstation.

## CONCLUSION

We have shown that SW analysis is an effective approach to estimate $V_P$ static corrections, which are necessary to obtain an accurate seismic image of mineralization targets. Since the only input to the proposed method are the seismic reflection data, the acquisition of which is usually not optimized for SW analysis, we have shown that SWs are a useful by-product. The successful results of the proposed example from the

iron-oxide mining site of Ludvika in Sweden, presented in this work, serve as proof of concept.

The proposed method is fully data driven and does not require any *a priori* information. It uses seismic noise (groundroll) and provides statics for P-wave seismic data in a fast way, compared with the conventional tomostatics approach, which requires first-break picking. It is faster than most typical SW methods, which makes it appropriate for large-scale applications and long seismic profiles. The workflow provided $V_P$ statics with mostly negligible difference with respect to statics computed through P-wave tomography. The quality of the resulting stacked image showed that they can be considered as a valid alternative to the conventional method.

## ACKNOWLEDGEMENTS

## ORCID

*Myrto Papadopoulou* (iD)
https://orcid.org/0000-0002-5112-2732
*Federico Da Col* (iD) https://orcid.org/0000-0002-1121-1001
*Binbin Mi* (iD) https://orcid.org/0000-0002-4317-3732
*Emma Bäckström* (iD)
https://orcid.org/0000-0003-0218-6411
*Paul Marsden* (iD) https://orcid.org/0000-0002-3862-4703
*Bojan Brodic* (iD) https://orcid.org/0000-0003-4694-9847
*Alireza Malehmir* (iD) https://orcid.org/0000-0003-1241-2988
*Laura Valentina Socco* (iD)
https://orcid.org/0000-0001-8830-9050

## REFERENCES

Aki K. and Richards P.G. 1980. *Seismology. Theory and Methods.* W.H. Freeman & Co.

Balestrini F., Draganov D., Malehmir A., Marsden P. and Ghose R. 2020. Improved target illumination at Ludvika mines of Sweden through seismic-interferometric surface-wave suppression. *Geophysical Prospecting* **68**, 200–213.

Bergamo P., Comina C. and Maraschini M. 2011. Seismic characterization of shallow bedrock sites with multimodal Monte Carlo inversion of surface wave data. *Soil Dynamics and Earthquake Engineering* **31**, 530–534.

Bergamo P. and Socco L.V. 2014. Detection of sharp lateral discontinuities through the analysis of surface-wave propagation. *Geophysics* **79**, EN77–EN90.

Bohlen T., Kugler S., Klein G. and Theilen F. 2004. 1.5D inversion of lateral variation of Scholte-wave dispersion. *Geophysics* **69**, 330–344.

Boiero D., Marsden P., Esaulov V., Zarkhidze A. and Vermeer P. 2011. Building a near-surface velocity model in the South Ghadames Basin: surface-wave inversion to solve complex statics. SEG Technical Program, Houston, USA, Expanded Abstracts, 1811–1815.

Boiero D. and Socco L.V. 2010. Retrieving lateral variation from surface wave dispersion curve analysis. *Geophysical Prospecting* **58**, 977–996.

Bräunig L., Buske S., Malehmir A., Bäckström E., Schön M. and Marsden P. 2020. Seismic depth imaging of iron-oxide deposits and their host rocks in the Ludvika mining area of central Sweden. *Geophysical Prospecting* **68**, 24–43.

Buske S., Bellefleur G. and Malehmir A. 2015. Introduction to special issue on "hard rock seismic imaging". *Geophysical Prospecting* **63**, 751–753.

Casto D.W., Luke B., Calderon-Macias C. and Kaufmann R. 2009. Interpreting surface-wave data for a site with shallow bedrock. *Journal of Environmental and Engineering Geophysics* **14**, 115–127.

Cercato M., Cara F., Cardarelli E., Di Filippo G., Di Giulio G. and Milana G. 2010. Shear-wave velocity profiling at sites with high stiffness contrasts: a comparison between invasive and non-invasive methods. *Near Surface Geophysics* **8**, 75–94.

Colombero C., Cojocariu E.I., Comina C. and Socco L.V. 2017. Imaging of sharp lateral variations in the subsoil: a numerical comparison of surface-wave based methods. GNGTS 2017, Expanded Abstracts, 688–693.

Cox M.J.G. 1999. *Static Corrections for Seismic Reflection Surveys.* Tulsa, OK: Society of Exploration Geophysicists.

Douma H. and Haney M. 2011. Surface-wave inversion for near-surface shear-wave velocity estimation at Coronation field. SEG Technical Program, San Antonio, USA, Expanded Abstracts, 1411–1415.

Eaton D.W., Milkereit B. and Salisbury M.H. 2003. Hardrock seismic exploration: mature technologies adapted to new exploration targets. In: *Hardrock Seismic Exploration* (eds. Eaton D.W., Milkereit B. and Salisbury M.H.), pp. 1–6. SEG.

Foti S., Hollender F., Garofalo F., Albarello D., Asten M., Bard P.Y., *et al.* 2018. Guidelines for the good practice of surface wave analysis: a product of the InterPACIFIC project. *Bulletin of Earthquake Engineering* **16**, 2367–2420.

Foti S., Lai C.G., Rix G.J. and Strobbia C. 2014. *Surface Wave Methods for Near-Surface Site Characterization.* CRC Press.

Gercek J. 2007. Poisson's ratio values for rocks. *International Journal of Rock Mechanics and Mining Sciences* **44**, 1–13.

Górszczyk A., Malinowski M. and Bellefleur G. 2015. Enhancing 3D post-stack seismic data acquired in hardrock environment using 2D curvelet transform. *Geophysical Prospecting* **63**, 903–918.

Harrison C.B., Urosevic M. and Stoltz E. 2007. Processing and seismic inversion of the Intrepid seismic line at the St. Ives gold camp, Western Australia. *Proceedings of Exploration 07: Fifth Decennial International Conference on Mineral Exploration*, 1087–1090.

Heinonen S., Kukkonen I., Heikkinen P. and Schmitt D. 2011. High resolution reflection seismics integrated with deep drill hole data in Outokumpu, Finland. *Geological Survey of Finland, Special Paper* **51**, 105–118.

Hollis D., McBride J., Good D., Arndt N., Brenguier F. and Olivier G. 2018. Use of ambient noise surface wave tomography in mineral resource exploration and evaluation. SEG Technical Program, Anaheim, USA, Expanded Abstracts, 1937–1940.

Ivanov J., Miller R. and Peterie S. 2016. Detecting and delineating voids and mines using surface wave methods in Galena, Kansas. SEG Technical Program, Dallas, USA, Expanded Abstracts, 2344–2350.

Karimpour M. 2018. *Processing workflow for estimation of dispersion curves from seismic data and QC*. MSc thesis, Politecnico di Torino, Italy.

L'Heureux E., Milkereit B. and Adam E. 2005. 3D seismic exploration for mineral deposits in hardrock environments. *Recorder* **30**, 36–39.

Malehmir A., Durrheim R., Bellefleur G., Urosevic M., Juhlin C., White D.J., *et al.* 2012. Seismic methods in mineral exploration and mine planning: a general overview of past and present case histories and a look into the future. *Geophysics* **77**, WC173–WC190.

Malehmir A., Maries G., Bäckström E., Schön M. and Marsden P. 2017. Developing cost-effective seismic mineral exploration methods using a landstreamer and a drophammer. *Scientific Reports* **7**, 10325.

Maraschini M., Boiero D. and Socco L.V. 2009. P and S wave velocity model retrieved by multi modal surface wave analysis. *71st EAGE Conference and Exhibition*, Amsterdam, The Netherlands, Expanded Abstracts, T010.

Maries G., Malehmir A., Bäckström E., Schön M. and Marsden P. 2017. Downhole physical property logging for iron-oxide exploration, rock quality, and mining: an example from central Sweden. *Ore Geology Reviews* **9**, 1–13.

Markovic M., Maries G., Malehmir, A., von Ketelholdt J., Bäckström E., Schön M. 2020. Deep reflection seismic imaging of iron-oxide deposits in the Ludvika mining area of central Sweden. *Geophysical Prospecting* **68**, 7–23.

Marsden D. 1993. Static corrections—a review, Part 1. *The Leading Edge* **12**, 43–49.

Miao X., Zheng D., Zi L., Zhou Z. and Meng G. 2016. Robust multimodal surface-wave inversion for shallow velocity and shear statics. SEG Technical Program, Dallas, USA, Expanded Abstracts, 4956–4960.

Nasseri-Moghaddam A., Cascante G. and Hutchinson J. 2005. A new quantitative procedure to determine the location and embedment depth of a void using surface waves. *Journal of Environmental and Engineering Geophysics* **10**, 51–64.

Nedimović M.R. and West G.F. 2003. Crooked-line 2D seismic reflection imaging in crystalline terrains: Part 1, data processing. *Geophysics* **68**, 274–285.

Park C.B., Miller R.D. and Xia J. 1998. Imaging dispersion curves of surface waves on multi-channel record. SEG Technical Program, New Orleans, USA, Expanded Abstracts, 1377–1380.

Pileggi D., Rossi D., Lunedei E. and Albarello D. 2011. Seismic characterization of rigid sites in the ITACA database by ambient vibration monitoring and geological surveys. *Bulletin of Earthquake Engineering* **9**, 1839–1854.

Rector J.W., Pfeiffe J., Hodges S., Kingman J. and Sprott E. 2015. Tomographic imaging of surface waves: a case study from the Phoenix Mine, Battle Mountain, Nevada. *The Leading Edge* **34**, 1360–1364.

Richart Jr. F.E., Hall Jr. J.R. and Woods R.D. 1970. *Vibrations of Soils and Foundations*. Englewood Cliffs, NJ: Prentice Hall.

Roberts B., Zaleski E., Adam E., Perron G., Petrie L., Drach W., *et al.* 1997. Seismic exploration of Manitouwadge Greenstone Belt, Ontario. *Proceedings of Exploration 97: Fourth Decennial International Conference on Mineral Exploration*, 451–454.

Rogers A.W. 1981. Determination of static corrections. In: *Developments in Geophysical Exploration Methods. The Developments Series* (ed. A.A. Fitch). Springer.

Saunders S., Lamb P. and Sweeney D. 1991. High resolution seismic for resolving coal seam structure in difficult terrain. *Geophysics* **22**, 325–332.

Sharma H., Hollis D. and McBride J. 2018. Application of ambient noise analysis and velocity modeling in mineral exploration. SEG Technical Program, Anaheim, USA, Expanded Abstracts, 3072–3076.

Sherman C., Rector J., Dreger D. and Glaser S. 2014. Seismic tunnel detection at Black Diamond Mines Regional Preserve. SEG Technical Program, Denver, USA, Expanded Abstracts, 2078–2082.

Socco L. and Comina C. 2017. Time-average velocity estimation through surface-wave analysis: Part 2 – P-wave velocity. *Geophysics* **82**, U61–U73.

Socco L., Comina C. and Khosro Anjom F. 2017. Time-average velocity estimation through surface-wave analysis: Part 1 – S-wave velocity. *Geophysics* **82**, U49–U59.

Socco L.V. and Boiero D. 2008. Improved Monte Carlo inversion of surface wave data. *Geophysical Prospecting* **56**, 357–371.

Socco L.V., Boiero D., Foti S. and Wisén R. 2009. Laterally constrained inversion of ground roll from seismic reflection records. *Geophysics* **74**, G35–G45.

Soumya R., Stewart R.R. and Al Dulaijan K. 2010. S-wave velocity and statics from ground-roll inversion. *The Leading Edge* **29**, 1250–1257.

Urosevic M., Kepic A., Stolz E. and Juhlin C. 2007. Seismic exploration of ore deposits in Western Australia. *Proceedings of Exploration 07: Fifth Decennial International Conference on Mineral Exploration*, 525–534.